Submitted: 12. 08. 2023.

Accepted: 08. 09. 2023.

SYNTHESIS, CHARACTERIZATION AND ELECTROCHEMICAL PROPERTIES OF IRON DOPED PHOSPHATE TUNGSTEN HETEROPOLY ACID (Fe-PWA) AND IT'S BRONZE (Fe-PWB): COMPARATIVE STUDY

Jovana Ackovic[1], Ružica Micic[1], Zoran Nedic[2], Tamara Petrovic[2], Jelena Senćanski[3], Maja Pagnacco[4*], Pavle Tančić[4]

[1] University of Priština in Kosovska Mitrovica, Faculty of Sciences and Mathematics, Department of Chemistry, Lole Ribara 29, 38220 Kosovska Mitrovica, Serbia

[2] Faculty of Physical Chemistry, University of Belgrade, Studentski trg 12-16, 11000 Belgrade, Serbia

[3] Institute for General and Physical Chemistry, University of Belgrade, Studentski trg 12-16, 11000 Belgrade, Serbia

[4] University of Belgrade, Institute of Chemistry, Technology and Metallurgy, Department of Catalysis and Chemical Engineering, Njegoševa 12, 11000 Belgrade, Serbia

[*]*E-mail address of the corresponding Author: Maja Pagnacco, Institute of Chemistry, Technology and Metallurgy, University of Belgrade, Njegoševa 12, 11000 Belgrade, Serbia, maja.pagnacco@ihtm.bg.ac.rs or maja.milenkovic@ymail.com*

https://doi.org/10.2298/SOS230812053A

Abstract: *In this work, synthesized 12-tungstenphosphoric acid ($H_3PW_{12}O_{40} \times nH_2O$; PWA) was further ionically exchanged with Fe^{3+} ions, which led to the formation of the 12-tungstophosporic acid iron salt, ($FePW_{12}O_{40} \times nH_2O$; Fe-PWA). Fe-PWA was then subjected to thermal analysis (TGA/DTA), determining the phase transition temperature of 576 °C from Fe-PWA to its corresponding phosphate tungsten bronze doped with iron, Fe-PWB. Using the X-ray powder diffraction (XRPD), Fourier-transform infrared spectroscopy (FTIR), and Scanning electron microscopy with an energy dispersive X-ray spectroscopy (SEM-EDS) method, the obtained Fe-PWA and Fe-PWB were additionally characterized, and compared. Due to channels and cavities in their structures, Fe-PWA and Fe-PWB were next examined as electrode materials for aqueous rechargeable batteries. Electrochemical measurements were done in aqueous solutions of 6 M $LiNO_3$ by cyclic voltammetry. Fe-PWA and Fe-PWB exhibit different redox processes, which are discussed thoroughly in this work. Electrochemical results are showing that within the Fe-PWA structure, more Li^+ ions can be intercalated in the first discharge cycle, but consecutive cycling leads to a fast capacity fade. While the Fe-PWB redox process was stable during cycling, its specific capacity is limited by the material's poor electrical conductivity. Improvements in Fe-PWB conductivity must be addressed in future studies in order to boost material's electrochemical performance.*

***Keywords**: Heteropoly compound; 12-tungstophosporic acid iron salt, Iron phosphate tungsten bronze; Keggin anion; Cyclic voltammetry; Lithium intercalation/deintercalation reaction.*

1. Introduction

Due to the interesting chemical, optical, electrical, and mechanical properties, tungsten compounds, especially tungsten bronzes, have been extensively studied in numerous technological applications, e.g., pigments in traditional ceramics, switches in optical networks, components of quantum computers, fluorescent markers, chemical sensors in different electric, and electrochromic devices, as mechanical components in anticorrosion fibers, cosmetic industry, electrocatalysis, and Li^+-ion batteries [1-7].

Phosphate-tungsten bronzes (PWBs) were obtained by thermal treatment of heteropoly compound 12-tungstenphosphoric acid ($H_3PW_{12}O_{40} \times nH_2O$) and their salts ($PWA \times nH_2O$; n = 29, 21, 14 and 6). Namely, the basic structural unit of PWA is the Keggin's anion $[PW_{12}O_{40}]^{3-}$ consisting of the central PO_4^{3-} tetrahedron surrounded by twelve WO_6 octahedrals [8,9]. Keggin anions are interconnected by hydrogen-bonded water molecules. By heat treatment at the temperature of about 600 ^oC, Keggin anion collapse and PWA goes through solid phase transition and transforms into phosphate tungsten bronze. Such transformation is characterized primarily by losing water molecules, and by replacement of WO_6 octahedra with monophosphate (PO_4) or diphosphate (P_2O_7) groups [10-13]. Metal-doped phosphate tungsten bronzes (M*x*–PWB; M*x*–metal; $1 \leq x \leq 3$) can be produced in a very wide range of compositions since about 50 elements of the Periodic Table of the elements could be incorporated in 12-tungstenphosphoric heteropoly acid, obtaining the salts, which are afterwards thermally treated. Metal-phosphate tungsten bronzes with different structural arrangements can be produced if WO_6 units are replaced with mono-phosphate (PO_4) or di-phosphate (P_2O_7) groups [14,15]. Three main families are described: monophosphate tungsten bronzes, $A_x(PO_2)_4(WO_3)_{2m}$, either with (i) pentagonal tunnels ($MPTB_p$) or with (ii) hexagonal tunnels ($MPTB_h$), and (iii) diphosphate tungsten bronzes, $A_x(P_2O_4)_2(WO_3)_{2m}$, mainly with hexagonal tunnels ($DPTB_h$) [16]. This work deals with transition metal doped monophosphate tungsten bronzes $A_x(PO_2)_4(WO_3)_{2m}$.

Phosphate tungsten acids, PWA, their salts and bronzes, PWB, possess distinct and unusual physicochemical properties which make them suitable for various applications. The structure of tungsten phosphate acids, as discussed previously [17], consists from Keggin anions which are interconnected by hydrogen-bonded water

molecules. Such a structure is the cause of high ionic and electric conductance of PWA. Crystal water together with Keggin anions provides channels in PWA structure which could be used for ionic transport, as well as for intercalation reaction in battery systems. However, previous studies demonstrated the instability of Keggin type anion in aqueous media and in a wide range of organic solvent [18,19]. The dissolution of PWA may be prevented by doping with larger cations than H^+ and thus obtaining tungsten phosphate salts. On the other hand, tungsten phosphate bronzes are stable in aqueous and organic media and also, as previously mentioned, they possess tunnels (channels) in their structure that allow ions such as Li^+, Na^+, K^+, and others to transport and intercalate within their structure [20,21]. Aside from the structural advantages of PWA and PWB, the high oxidation state of tungsten (W^{6+}) in the structure of these compounds, prompted their investigation into electrode materials for secondary batteries.

Iron is one of the most abundant elements on Earth and the fourth-most abundant element in the Earth's crust. Namely, iron makes up more than 85% of the mass of the Earth's core and about 5% of the mass of the Earth's crust [22-24]. In living systems, it is one of the key microelements. Iron has a redox process that can favorably affect the electrochemical properties. Present Fe in its high oxidation state (i.e., +3) in our samples could facilitate more Li^+ on the account of its redox process. Therefore, in this work the phosphate tungsten heteropoly acid is doped with Fe^{+3} in order to investigate and compare electrochemical properties of salt Fe-PWA and its thermally obtained bronze Fe-PWB, for potential application as an electrode material for aqueous rechargeable batteries due to the channels and cavities present in their structure. Since Fe-PWA and Fe-PWB are the novel synthesized materials, they are primarily characterized by thermal techniques (TGA/DTA), X-ray powder diffraction (XRPD) method, Fourier Transform Infrared Spectroscopy (FTIR), and Scanning Electron Microscopy with an Energy Dispersive X-ray Spectroscopy (SEM-EDS) method.

2. Materials and Experimental Procedures

2.1 Synthesis of Fe-PWA and Fe-PWB

The 12-tungstenphosphoric heteropoly acid ($H_3PW_{12}O_{40} \times 29H_2O$) was synthesized as follows: dissolve 100g of $Na_2WO_4 \times 2H_2O$ (Carl Roth, Germany) in 100ml of water and carefully add 10 ml of 85% (ρ=1.70 g/cm^3) H_3PO_4 (Merck) and 80

ml of 37% (ρ=1.19 g/cm^3) HCl (Merck) previously mixed. A white precipitate is formed, which is a heteropolycation. The solution is filtered and the precipitate is transferred to a beaker and dissolved in 100 ml of water. This solution was transferred to a separatory funnel and 70 ml of ether (Carlo Erba, France) and 40 ml of 37% (ρ=1.19 g/cm^3) HCl were added. Three phases are separated, with the bottom phase representing the heteropolyacid solution. The lower layer is dropped into the vegeglass and left to crystallize. In this way, colorless, transparent crystals of $H_3PW_{12}O_{40} \times nH_2O$ (PWA) were obtained [25]. The dehydration process of PWA is done by its heating in a kiln at 80 °C and drying for 10 minutes [10]. Total return of PWA is about 60%.

In this paper, 12-tungstenphosphoric acid (PWA) was synthesized in combination with $FeCl_3$ at room temperature (25 ^oC). At such manner, Fe^{3+} ion exchange gave new 12-tungstenphosphoric salt of the transition metal iron ($Fe^{3+}PW_{12}O_{40} \times nH_2O$; Fe-PWA). Previous thermal analysis determined the temperature of about 600 ^oC of the phase transition, i.e., the temperature at which the structure of the Kegin anion is disturbed [10]. Therefore, it was chosen temperature above the breakdown of the Kegin anion of 650 ^oC, and which is required to obtain phosphate tungsten bronze (PWB) doped with iron (Fe-PWB). The sample was kept in the oven for 10 minutes.

2.2 Thermal analyses (TA)

Thermal examinations were performed using TA Instruments STD 2960 Simultaneous DSC-TGA using a higher scanning rate (10°C min^{-1}), from room temperature to 800°C in a stream of nitrogen.

2.3 X-ray powder diffraction (XRPD)

The XRPD patterns were obtained using a Rigaku Ultima 4 automated diffractometer with a Cu tube operating at 40 kV and 40 mA. The instrument was provided with a curved graphite monochromatic diffraction beam, and Xe-filled proportional counter. The diffraction data were collected in the 2θ Bragg angle ranges from 10 to 90^o, counting for 2 deg min^{-1} at every 0.05^o steps. The divergence and receiving slits were fixed at 0.5° and 0.15 mm, respectively. The XRPD measurements

were performed ex situ at room temperature (23 ^{o}C) in a stationary sample holder. Diffractometer alignment was checked by means of a standard Si powder material.

2.4 Fourier Transform Infrared Spectroscopy (FTIR)

FTIR spectra were recorded on a Thermo Scientific Nicolet 6700 using KBr pellet technique with 64 scan and 2 cm^{-1} resolution.

2.5 Scanning Electron Microscopy and Energy Dispersive X-ray Spectroscopy (SEM-EDS)

The images of film samples were examined by means of a JEOL 840A instrument equipped with EDS analyzer. The Fe-PWA and Fe-PWB samples were gold-coated for the SEM-EDS study.

2.6. Electrochemical measurements

Working electrodes for electrochemical investigations were prepared by making a suspension of Fe-PWA/Fe-PWB sample as the active material (85%), carbon black (10%) as the conductivity levelling additive, and polyvinylidene fluoride (PVDF) as the binder (5%) in the N-methyl-2-pyrrolidone solvent. After homogenization in an ultrasonic bath, the suspension was deposited on an electrically conducting support – glassy carbon (GC) electrode. It was dried in a vacuum oven for 4 h at 120 °C to evaporate the solvent. Cyclic voltammetry experiments were carried out in a three-electrode cell at room temperature, using a Gamry PCI4/300 Potentiostat/Galvanostat. The three-electrode cell was composed of a working electrode, a wide platinum foil as a counter electrode, and a saturated calomel electrode (SCE) as the reference electrode. The electrolyte was a saturated aqueous solution of $LiNO_3$ (6 M).

3. Results and Discussion

3.1 Characterization of Fe-PWA and Fe-PWB

The results of thermogravimetric (TGA) and differential thermal analysis (DTA) curves of $Fe^{3+}PW_{12}O_{40} \times nH_2O$ from room temperature to 900 ^{o}C are presented in Figure 1. DTA curve shows three endothermic peaks at 86 ^{o}C, 124 ^{o}C, 184 ^{o}C; and one exothermic peak at 576 ^{o}C, as may be observed. The weight loss up to ~450 ^{o}C

could result from the dehydration reaction of $Fe^{3+}PW_{12}O_{40} \times nH_2O$. If we suppose that mentioned dehydration reaction occurs as follows:

$$Fe^{3+}PW_{12}O_{40} \times zH_2O \rightarrow Fe^{3+}PW_{12}O_{40} + zH_2O,$$

then the water content, *z*, of the Fe-PWA sample can be roughly estimated using the following equation (1):

$$\frac{m_{H_2O}}{m_{FePW_{12}O_{40}xzH_2O}} = \frac{n_{H_2O}M_{H_2O}}{n_{FePW_{12}O_{40}}M_{FePW_{12}O_{40}} + n_{H_2O}M_{H_2O}} = \frac{zM_{H_2O}}{M_{FePW_{12}O_{40}} + zM_{H_2O}} \quad (1)$$

where $m_{FePW_{12}O_{40}xzH_2O}$ is mass at the beginning of TG measurements, m_{H_2O} is the mass loss recorded on the TG curve during dehydration, and M_{H_2O} and $M_{FePW_{12}O_{40}}$ are the molar masses of water and dehydrated $Fe^{3+}PW_{12}O_{40}$, respectively.

The first weight loss of ~8% up to 200 ^oC on TGA curve relates to water liberation adequate to the 13 moles of H_2O from the Fe-PWA hydrous structure. The second weight loss of ~0.95% in temperature range from 200 ^oC to 450 ^oC corresponding to the 2 moles of H_2O, and can be related to the liberation of crystal water from the Fe-PWA lattice. Therefore, it could be speculated that $FePW_{12}O_{40}$ has 15 moles of H_2O in its structure ($FePW_{12}O_{40} \times 15H_2O$). It should be emphasized here that positions of these endothermic peaks are different in comparison with the PWA [10] and Ca-PWA [26] phases, which have two endothermic peaks at considerable smaller temperatures of 50 ^oC and 170 ^oC. Furthermore, Fe-PWA also differs from the recently studied Ce-PWA and Pr-PWA, which are showing three endothermic peaks at 60 °C, 180 °C (doublet), and 340 °C [27].

On the other hand, it seems that at 450 ^oC anhydrous Fe-PWA was formed, and it was found to be stable up to about 600 ^oC. Namely, the exothermic solid-solid structural phase transformation from anhydrous heteropoly acid iron salt to iron doped phosphate tungsten bronze Fe-PWB occurred at 576 ^oC, which is very similar to the 602 ^oC, 590 ^oC and ~600 ^oC of PWB [10], Ca-PWB [26], and Ce-PWB and Pr-PWB [27] phases, respectively.

Figure 1.

The observed XRPD patterns of Fe-PWA and Fe-PWB are shown in Fig. 2 and Table I. As it was expected from our previous studies [10, 20, 21, 26, 27], it is obvious that these two phases are different among each other, confirming the solid-solid structural phase transformation observed by the thermal analysis (Fig. 1). Furthermore, the Fe-PWA phase pattern is different with the PWA [10] and Ca-PWA [26] phases, most probably to the determined different water contents (see discussion concerning TGA/DTA analyses). On the contrary, the Fe-PWB phase pattern is very similar to the previously characterized monoclinic PWB [10], Ca-PWB [26], Re-PWB [21], and Ce-PWB and Pr-PWB [27] bronzes; further indicating that all of these bronzes are structurally isomorphic. Calculations of the unit cell parameters of Fe-PWB were accomplished by the Rietveld refinement method and Fullprof program [28], and presented in Table II.

Figure 2.

Table I.

Table II.

When Fe was inserted into the structure of Fe-PWB, expansion of the unit-cell dimensions of PWB indeed occurred that may be observed from the results presented (Table II). Namely, it can be seen that inserting of the Fe^{3+} ion into the PWB's structure have the most influence to the axis a_0 and volume V_0 (i.e., they significantly increased) and angle β_0 (i.e., it significantly decreased). On the other hand, influence to the axis c_0 is quite smaller (i.e., it slightly decreased), whereas influence to the axis b_0 is minor.

The characteristic bands of Kegins anionic structure, which are related to the vibrations of H_2O molecules, PO_4 tetrahedra, and WO_6 octahedra may be observed in Fe-PWA spectrum (Fig. 3a and Table III). The band at 3330 cm^{-1} corresponds to stretching water vibrations, ν_1 (H_2O) [29], while the band at 1615 cm^{-1} corresponds to bending water vibrations, ν_2 (H_2O) [30]. The typical vibrations of PO_4 tetrahedrons are bands positioned at 1075 cm^{-1}, 973 cm^{-1}, and 595 cm^{-1}, while the typical vibrations of WO_6 octahedra are bands at 894 cm^{-1} and 785 cm^{-1} [26,31]. The characteristic vibration of the bond that connects PO_4 tetrahedrons and WO_6 octahedra (W-PO_4) is positioned at 426 cm^{-1} [31]. In the Fe-PWA spectra, shoulder at 1699 cm^{-1} becomes evident

compared to the Ca-PWA [26] spectra. The shoulder was assigned to the vibrations of H_3O^+ groups and was also present in the spectra of 29-PWA [10, 32]. Definite changes in water bands are related to the different numbers of water molecules (Fe-PWA×15H_2O, PWA×29H_2O [10, 32], and Ca-PWA×6H_2O [26]) and protonic species (H_3O^+, $H_5O_2^+$, etc.) present in the sample structure. Higher amounts of water molecules, as well as present protonic species, will alter heteropoly salt conductivity, making it more conductive among other less hydrated salts [32]. Going further with comparison, one may deduce coupling of the two vibrations related to the PO_4 units (973 cm^{-1}) and the W=O bond (894 cm^{-1}). These two bands are well defined in PWA [33] and Ca-PWA [26] spectra, while in Fe-PWA spectra they become one double-structured band. Also, a shift towards a lower wavenumber for bands corresponding to W=O and the W-O-W group was detected when cations were inserted in the PWA structure. This may lead to a weakening of the bonds within the WO_6 octahedron in the order PWA>Ca-PWA>Fe-PWA, while interaction between PO_4 tetrahedrons and WO_6 octahedra (W-PO_4) becomes stronger in the order PWA<Ca-PWA<Fe-PWA.

Figure 3.

Table III.

After the calcination process, definite changes in the FTIR spectra are also evident. Namely, the collapse of Kegin's anion (complete liberation of water molecules and rearrangement of PO_4 and WO_6 units) occurred, and Fe-PWB bronze was formed (Fig. 3b and Table III). The band at 1129 cm^{-1} is characteristic vibration of the PO_4 tetrahedra [26]. A band at 1030 cm^{-1}, and a very strong band at 754 cm^{-1} are characteristic bands of WO_6 octahedra [26]. The band positioned at 415 cm^{-1} corresponds to the characteristic vibration of the W-PO_4 unit. By comparing the FTIR spectra of Fe-PWB to those of PWB [31] and Ca-PWB [26], one may deduce that all bands in the FTIR spectra of Fe-PWB were slightly shifted. As it was mentioned previously, the type and nature of cations influence changes in FTIR spectra. The bands that showed the most obvious shift corresponds to characteristic vibrations of the O-W-O group (shifts towards lower wavenumbers) and the W-PO_4 group (shifts towards higher wavenumbers). Accordingly, the same conclusion was made even after formation of bronze, i.e., Fe-PWB is thought to have weaker bonds within WO_6 octahedrons but a stronger W-PO_4 bonds compared to PWB and Ca-PWB bronze.

Based on the comparative SEM-EDS analyses of the Fe-PWA and Fe-PWB phases in the selected regions and as linescans, as well (Fig. 4 and Table IV), different atomic and weight concentrations of elements W, O, P and Fe are quite evident. The reason for this could be obviously inhomogeneous distribution of the particles in the studied samples. Furthermore, the very interesting fact is that W and O are inversely related, whereas P and Fe show minor and almost constant variations (Figs. 4b and 4d). Fe-PWB is much more homogeneous than the Fe-PWA phase, because it has more similar region and linescan analyses (see Table IV), that could be also significant. Nevertheless, such results undoubtedly confirmed entering of the Fe^{3+} into the both Fe-PWA and Fe-PWB structures, in a very good agreement with the XRPD and FTIR analyses.

Figure 4.

Table IV.

3.2. Results of electrochemical measurements: Comparative cyclovoltammetry investigations of Fe-PWA and Fe-PWB

The initial electrochemical characterization of Fe-PWA and its related bronze, Fe-PWB, was examined using cyclic voltammetry in order to investigate their electrochemical activity and mechanism of intercalation/deintercalation of lithium ions. Comparative cyclic voltammetry investigations of Fe-PWA and its corresponding bronze, Fe-PWB, were done in an aqueous solution of $LiNO_3$ (6 M). Cyclic voltammograms (CVs) of Fe-PWA, measured in the potential range from +0.3 to −1 V versus SCE at a scan rate of 20 mV s^{-1}, and Fe-PWB, measured in the potential range from +0.5 to −0.9 V versus SCE at a scan rate of 20 mV s^{-1}, are presented in Figs. 5 and 6.

The distinction in CVs is caused by the structural difference between Fe-PWA and Fe-PWB. By comparing the CVs on Figs. 5a and 6a, it is possible to establish that both Fe-PWA (25.75 mAh g^{-1}) and Fe-PWB (2.39 mAh g^{-1}) exhibit low initial discharge capacity, which can be predicted due to the previously determined micrometer particle size (see Figs. 4a and 4c). Namely, particles of several μm have a low value of specific surface, which means that only a small number of Li-ions may be intercalated into the

sample structures [34]. Going further with the comparison, Fe-PWA can accommodate more Li^+ ions within various energetically different intercalation sites during the first discharge process compared to Fe-PWB. Fe-PWA's initial enhanced electrochemical activity compared to Fe-PWB is probably a consequence of the presence of crystal water and protonic species in the Fe-PWA structure, which provides additional sites for ion intercalation and enhances Fe-PWA's conductivity [18, 32]. Also, a slightly higher specific capacity of Fe-PWA could be linked to a higher number of agglomerated particles, which are holding tighter together and ensuring better contact among them, providing an increased diffusion path for ions [34]. On the other hand, Fe-PWB is definitely more stable during further cycling. As a result, they will be discussed separately in the following paragraph.

Figure 5.

Figure 6.

The CV of Fe-PWA, shown in Fig. 5a, is composed of five cathodic peaks located at -0.09, -0.31, -0.54, -0.70, and -0.90 V vs. SCE. Li^+ ions are considered to be intercalated within the five available intercalation sites in the Fe-PWA structure during the first reduction process. Fully lithiated bronze, $FeLi_x$-PWA, is probably obtained at the end of the reduction process. The specific discharge capacity calculated from the CV is 25.72 mAh g^{-1}. The first oxidation, i.e., deintercalation process, is followed by the appearance of low-intensity anodic peaks positioned at -0.84, -0.65, -0.20, and -0.12 V vs. SCE. Upon the first release of intercalated Li^+ ions, an irreversible reaction occurred, causing the detachment and dissolving of some of the material deposited on the GC electrode in the electrolytic solution (see inset in Fig. 5a). The retained value of the specific capacity after the first deintercalation process was only 2.88 mAh g^{-1} (89% capacity loss). Except for the cathodic peak at -0.54 V vs. SCE, which has no anodic pair, all four cathodic peaks have their own anodic pair on the CV. At potentials of the cathodic peak without its anodic pair, -0.54 V vs. SCE, the specific current was highest, possibly due to the highest number of Li^+ ions incorporated at that intercalation site. During the second reduction process, Fig. 5b shows the disappearance of the cathodic peak positioned at -0.54 V vs. SCE, implying that the deintercalation of Li^+ ions at -0.54 V vs. SCE led to a rapid structural collapse of Fe-PWA. Storing a high number of Li^+

ions within the same intercalation site may promote repulsive interactions between neighboring Li^+ ions, which could lead to an increase in the volume of the unit cell and an irreversible structural change [35]. As cycling continued, the loss in stability of Fe-PWA was still present. Taking into account the present Keggin type of anion in the Fe-PWA structure, its electrochemical instability during intercalation/deintercalation processes in an aqueous solution could be related to the formation of lithiated Fe-PWA phases, which promote the collapse of the Keggin type of anion and make Fe-PWA highly solubilized in aqueous electrolytes [18]. Based on the obtained results, it could be concluded that Fe-PWA could not be used as the electrode material for aqueous Li-ion batteries, but Fe-PWA redox activity should be examined in other electrolytes, especially nonaqueous electrolytes.

Unlike Fe-PWA, in which there are five available intercalation sites for Li^+ ion insertion, in the structure of Fe-PWB there are only two sites (two redox peaks) available for Li^+ ion intercalation/deintercalation at potentials of -0.3/-0.2 and -0.56/-0.69 V vs. SCE, Fig. 6a (more pronounced peaks at 5 mV s^{-1}, Fig. 6b). The reduced number of available sites for ion intercalation in Fe-PWB is probably the result of Keggin anion collapse and the release of crystalline water from the crystal structure. The specific capacity of Fe-PWB is low (2.96 mAh g^{-1} at discharging and 1.78 mAh g^{-1} at charging), but Fe-PWB is more stable during cycling compared to Fe-PWA.

Vujkovic et al. [20] investigated the intercalation kinetics of lithium in lithium-free (PWB) and lithium-doped bronzes (Li_3-PWB and Li_n-PWB) in an aqueous solution of $LiNO_3$. Vujkovic et al. also assigned redox peaks found in the CVs of PWB, Li_3-PWB, and Li_n-PWB [20] in aqueous Li-electrolyte to Li^+ ion intercalation/deintercalation reactions. The presence and the positions of the redox peaks among all mentioned tungsten bronzes, as well as the here investigated Fe-PWB, seem to depend on the type and amount of dopant in PWB. Namely, it was reported that PWB exhibits relatively fast and stable lithium insertion/disinsertion with sharp and noticeable redox peaks, while the other three samples exhibit sluggish kinetics with broad and barely visible peaks (especially in the case of Li_3-PWB and Li_n-PWB). The sluggish intercalation kinetics of lithium-doped phosphate tungsten bronzes originate from the corruption of PWB metallic behavior by electron filling the W-O-W hybridized π^* conduction band [14, 20, 35, 36] and changing the metallic behavior of

PWB to that of a semiconductor to an insulator. Accordingly, the low current response of the Fe-PWB sample is probably also due to the decreased electrical conductivity compared to the PWB sample. While Li-doped bronzes exhibit irreversible delithiation, which leads to fast capacity fade, Fe-PWB was stable during cycling and had a slightly higher specific capacity compared to Li-doped bronzes. All of the results point to the conclusion that Fe-doped bronzes, compared to Li-doped bronzes, exhibit greater electrochemical stability. Incorporating Fe^{3+} ions seems to protect the bronze structure from collapsing during Li^+ ion intercalation/deintercalation since there was no capacity fade with cycling. Since there is no available literature on Fe-doped bronzes, we may only assume that the higher electrochemical activity of Fe-PWBs in comparison to Li-doped bronzes can be explained with the $Fe^{3+} \leftrightarrow Fe^{2+}$ redox process [24]. Namely, Fe^{3+} ions, besides W^{5+} ions, may undergo the redox process $Fe^{3+} \leftrightarrow Fe^{2+}$ which enables the intercalation/deintercalation of a higher number of Li^+ ions [37] within Fe-PWB's structure.

Martinez-de la Cruz et al. [36] investigated the electrochemical insertion of lithium from an organic electrolyte (e.g., 1 M $LiPF_6$ in EC/DMC (50:50)) solution into the monophosphate bronze structures – $(PO_2)_4(WO_3)_{2m}$ ($2 \leq m \leq 10$). During the first discharge cycle, they attained a very high specific capacity (625 mAh g^{-1}) up to a potential of 0 V vs. Li/Li^+. Further cycling caused a significant capacity fade, which is associated with: 1) irreversible structural transformation of the host matrix bronze and the appearance of two distinct phases: orthorhombic and monoclinic; and 2) lithium insertion, which led to a transition from metallic to insulator behavior in the examined bronzes [14, 36]. Electrochemical measurements done in this work were limited by the electrochemical window of an aqueous solvent. Considering the stability of Fe-PWB during intercalation/deintercalation reactions, it is desirable to further investigate Fe-PWB's electrochemical activity in organic electrolytes, which will expand the electrochemical window.

Metal-doped phosphate-tungsten bronzes (M*x*–PWB) have potential as an anode material in rechargeable batteries, but their electrochemical properties have to be improved. More research efforts should be implied for achieving the improvement of the doped bronze's electrical conductivity properties. As it has been shown in this work,

doping PWB with iron favourably affects the energy storage process probably due to iron's redox process. Further investigation may be directed towards doping PWB with another transition metal/metals that exhibit several oxidation states and also improve the metallic behaviour of doped tungsten bronzes, which could be essential for boosting electric capacity. Furthermore, optimising synthesis conditions or utilising an alternative synthesis process could improve the electrochemical characteristics of M*x*–PWB by increasing specific surface area and reducing particle size to nanometers. This goal could be accomplished by making M*x*–PWB composites using carbon or silica powder [38], which is a well-established method.

4. Conclusions

The thermally phase transformation of iron salt of 12-tungstophosphoric acid in order to obtain novel Fe-doped phosphate tungsten bronze has been presented and characterized in this work. Samples were further characterized by XRPD, FTIR, SEM-EDS and cyclic voltammetry methods. Based on the obtained characterization results, it was confirmed that Fe^{3+} ions fully entered into the heteropoly acid and bronze structures, as well as the success of the Fe-PWA and Fe-PWB synthesis. The distinctive structural characteristics of Fe-PWA and Fe-PWB, as well as the high oxidation states of iron and tungsten, have prompted investigation into their potential application as electrode materials in lithium-ion batteries. The electrochemical experiments conducted by cyclic voltammetry revealed that both the Fe-PWA and Fe-PWB samples exhibit a low specific capacity. However, because Fe-PWB has strong electrochemical stability during cycling, further enhancements to boost its specific capacity are needed, and this will be the focus of our future research.

Acknowledgments

This work was financially supported by the Ministry of Science, Technological Development and Innovation of the Republic of Serbia (Grants No. 451-03-47/2023-01/200146, 451-03-47/2023-01/200026, and 451-03-47/2023-01/200051) and Faculty of Science and Mathematics, University of Priština in Kosovska Mitrovica (Grant No. IJ-2301).

5. References

1. Patent (2005) US Appl. No. 11/125,316, filled 10 May 2005

2. E. Castel, P. Veber, M. Albino, M. Velazquez, S. Pechev, D. Denux, J. P. Chaminade, M. Maglione, M. Josse, J. Cryst. Growth 340 (2012) 156. https://doi.org/10.1016/j.jcrysgro.2011.11.082

3. I. Tsuyumoto, T. Kudo, Sens Actuators B 30 (1996) 95. https://doi.org/10.1016/0925-4005(95)01755-K

4. I. Holclajtner-Antunović, U. Mioč, M. Todorović, Z. Jovanović, M. Davidović, D. Bajuk-Bogdanović, Z. Laušević, Mater. Res. Bull 45 (2010) 1679. https://doi.org/10.1016/j.materresbull.2010.06.064

5. A. Martinez-de la Cruz, F. E. L. Rodriguez, J. Phys. Chem. Solids 69 (2008) 830. https://doi.org/10.1016/j.jpcs.2007.09.008

6. A. Martinez-de la Cruz, F. E. L. Rodriguez, L.T. Gonzales, L. M. T. Martinez, Electrochim. Acta 52 (2007) 6490. https://doi.org/10.1016/j.electacta.2007.04.045

7. R. M. Abozaid, Z. Ž. Lazarević, V. Radojević, M. S. Rabasović, D. Šević, M. D. Rabasović, N. Ž. Romčević, Sci. Sinter. 50 (2018) 445. https://doi.org/10.2298/SOS1804445A

8. J. F. Keggin, Proc. Roy. Soc. A144 (1934) 75.

9. C. J. Clark, D. Hall, Acta Cryst. B32 (1976) 1545.

10. U. B. Mioč, R. Ž. Dimitrijević, M. Davidović, Z. P. Nedić, M. M. Mitrović, Ph. Colomban, J. Mater. Sci. 29 (1994) 3705. https://doi.org/10.1007/BF00357338

11. R. Dimitrijević, U. B. Mioč, M. Davidović, M.R. Todorović, Z. Nedić, N. Tjapkin, Proc. Natural Sci. Matica Srpska 85 (1993) 329.

12. U. B. Mioč, R. Ž. Dimitrijević, M. M. Mitrović, Z. P. Nedić, J. Serb. Chem. Soc. 60 (1995) 959.

13.V. Jokanović, U. B. Mioč, Z. P. Nedić, Solid State Ion. 176 (2005) 2955. https://doi.org/10.1016/j.ssi.2005.09.029

14. A. Martinez-de la Cruz, F. E. L. Rodriguez, J. I. Rodriguez, Solid State Ion. 176 (2005) 2625. https://doi.org/10.1016/j.ssi.2005.08.009

15. F. E. L. Rodríguez, A. Martínez-de la Cruz, E. López Cuéllar, J. Power Sources. 160 (2006) 1314. https://doi.org/0.1016/j.jpowsour.2006.02.049

16. P. Roussel, O. Perez, Ph. Labbe, Acta Crystallog. B. 57 (2001) 603. https://doi.org/10.1107/S0108768101009685

17. Z. Jovanović, I. Holclajtner-Antunović , D. Bajuk-Bogdanović , S. Jovanovića, Ž. Mravik, M. Vujković, Electrochem. Commun. 83 (2017) 36. https://doi.org/ 10.1016/j.elecom.2017.08.017

18. I. Holclajtner-Antunović , D. Bajuk-Bogdanović , A. Popa, S. Uskoković – Marković, Inorg. Chim. Acta 383 (2012) 26. https://doi.org/10.1016/j.ica.2011.10.035

19. I. Holclajtner-Antunović, D. Bajuk-Bogdanović, M. Todorović, U. B. Mioč, J. Zakrzewska, S. Uskoković-Marković, Canadian Journal of Chemistry 10 (2008). https://doi.org/ 10.1139/v08-138

20. M. Vujković, Z. Nedić, P. Tančić, O. S. Aleksić, M. V. Nikolić, U. Mioč, S. Mentus, J. Mater. Sci. 51 (2016) 2481. https://doi.org/10.1007/s10853-015-9560-5

21. M. Pagnacco, S. Marković, J. Potočnik, V. Krstić, P. Tančić, M. Mojović, Z. Mojović, J. Electrochem. Soc. 169(10) (2022) 106508. https://doi.org/10.1149/1945-7111/ac96ab

22. D.Y. Pushcharovsky, Geochem. Int. 57 (2019)941. https://doi.org/10.1134/S0016702919090088

23. A. Pilchin, L.V. Eppelbaum, 1st ed.; Geoph. Society 2006; ISBN 970-32-4122-0. https://doi.org/10.3390/antibiotics10070884

24. F. Parast, M. Montazeri-Pour, M. Rajabi, F. Bavarsiha, Sci. Sinter. 52 (2020) 415. https://doi.org/10.2298/SOS2004415P

25. P. Kerserho, These, Universite Piere et Marie Curie, Paris 4 (1982).

26. T. V. Maksimović , J. P. Maksimović , P. I. Tančić , N. I. Potkonjak , Z. P. Nedić , Lj.G. Joksović, M. C. Pagnacco, Sci. Sinter. 53 (2021) 223. https://doi.org/10.2298/SOS2102223M

27. T. Maksimović, P. Tančić, J. Maksimović, D. Mara, M. Ilić, R. Van Deun, Lj. Joksović, M. Pagnacco, Optical Materials, 143 (2023). https://doi.org/ 10.1016/j.optmat.2023.114125

28. Rodriguez-Carvajal, J. Program Fullprof (Computer software). In Proceedings of the Abstract of 15th Conference of International Union of Crystallography, Satellite Meeting on Powder Diffraction, Toulouse, France, July 16-19th 1990; p. 127

29. S. Milanović, N. Potkonjak, V. Mandušić, Đ. Čokeša, J. Hranisavljević, B. Kaluđerović, Sci. Sinter. 52 (2020) 87. https://doi.org/10.2298/SOS2001087M

30. F. Parast, M. Montazari-Pour, M. Rajabi, F. Bavvarsiha, Sci. Sinter. 52 (2020) 415. https://doi.org/10.2298/SOS2004415P

31. Z. P. Nedić, (2016) The preparation and characterizationof phosphoroustungsten bronzes doped with lithium, magnesium and europium ions, PhD Thesis, University of Belgrade, Faculty of physical chemistry, Serbia. 108 pp.

32. U. Mioč, M. Davidović, N. Tjapkin, Ph. Colomban, A. Novak, Solid State Ion. 46 (1991) 103, https://doi.org/10.1016/0167-2738(91)90136-Y

33. C. T. Cavalcante, C. Molina, T. S. Martins, J. Mater. Sci.: Mater Electon. 30 (2019) 16903. https://doi.org/10.1007/s10854-019-01626-0

34. L. Bläubaum, F. Röder, C. Nowak, H.S. Chan, A. Kwade, U. Krewer, Chem. Electro. Chem. 7 (2020) 4755. https://doi.org/10.1002/celc.202001249

35. E. Wang, M. Greenblatt, J. Solid State Chem. 68 (1987), 38. https://doi.org/10.1016/0022-4596(87)90282-9

36. A. Martínez-de la Cruz, F.E.L. Rodríguez, Electrochim. Acta. 54 (2009) 3176. https://doi.org/10.1016/j.electacta.2008.11.056

37. Y. Liua, D. Liua, Q. Zhanga, D. Yua, J. Liuc, G. Caoa, Electrochim. Acta. 56 (2011) 2559. https://doi.org/10.1016/j.electacta.2010.11.050

38. V. Jokanovic, Z. Nedic, Ultrasonics Sonochemistry 17 (2010) 228. https://doi.org/10.1016/j.ultsonch.2009.05.007

Figure Captions:

Figure 1. TGA (red) and DTA (green) curves of $Fe^{3+}PW_{12}O_{40} \times nH_2O$

Figure 2. XRPD patterns of Fe-PWA (upper) and Fe-PWB (lower).

Figure 3. FTIR spectra of: (a) Fe-PWA and (b) Fe-PWB.

Figure 4. (a) SEM photo of the whole presented region and linescan (marked with black and white arrow) analyses of Fe-PWA; (b) combined EDS linescan analyses of Fe-PWA (W, O, P and Fe elements are marked with different colors); (c) SEM photo of the whole presented region and linescan (marked with black and white arrow) analyses of Fe-PWB; and (d) combined EDS linescan analyses of Fe-PWB (W, O, P and Fe elements are marked with different colors)

Figure 5. CVs of Fe-PWA: 1^{st} cycle, a), and 2^{nd} to 5^{th} cycles for a better view, b), measured at a scan rate of 20 mV s^{-1}, c), structural degradation of Fe-PWA followed by its dissolution after the first deintercalation process.

Figure 6. CVs of Fe-PWB measured at a scan rate of 20 mV s^{-1}, a), and 5 mV s^{-1}, b).

Tables:

Table I. Observed inter-planar spacings (d_{obs}, in Å) and intensities (I_{obs}, in %) of the Fe-PWA and Fe-PWB phases.

Fe-PWA		**Fe-PWB**	
d_{obs}	**I_{obs}**	**d_{obs}**	**I_{obs}**
11.107	45	3.763	100
10.051	28	2.663	70
8.624	55	2.180	14
5.000	17	1.874	10
4.298	25	1.685	22
3.848	16	1.538	13
3.513	100	1.333	5
3.243	13	1.254	6
3.038	36		
2.596	50		
2.388	23		
1.873	7		
1.718	25		
1.544	22		
1.494	7		

Table II. Calculated unit cell parameters of Fe-PWB, in comparison with PWB [8], Ce-PWB, Pr-PWB, Ca-PWB and Li-PWB [25], and Re-PWB [19] bronzes.

	Fe-PWB	**PWB**	**Ce-PWB**	**Pr-PWB**	**Ca-PWB**	**Li-PWB**	**Re-PWB**
a_0 (Å)	7.53(3)*	7.325(6)	7.45(1)	7.33(4)	7.442(4)	7.309(4)	7.35(8)
b_0 (Å)	7.51(1)	7.516(9)	7.518(5)	7.53(1)	7.497(7)	7.521(2)	7.52(5)
c_0 (Å)	7.64(2)	7.686(9)	7.630(5)	7.68(1)	7.646(3)	7.682(3)	7.68(2)
β_0 (^{o})	89.7(3)	90.79(5)	90.12(8)	90.9(2)	90.38(4)	89.84(6)	91.1(4)
V_0 (Å^3)	431(2)	423.1(9)	427.1(6)	424(2)	426.6(3)	422.3(3)	424(3)

*-The numbers in parentheses are the estimated standard deviations and refer to the last significant number

Table III. Characteristic frequencies of Fe-PWA and Fe-PWB.

Fe-PWA		**Fe-PWB**	
Wavenumber / cm^{-1}	**Assignation**	**Wavenumber / cm^{-1}**	**Assignation**
3330vs	ν_1 (H_2O)	/	
1699sh	ν (H_3O^+)	/	
1615m	ν_2 (H_2O)	/	
1075s	ν_3 (PO_4)	1129m	ν_3 (PO_4)
973s	ν_1 (PO_4)	/	
894m	ν (W=O)	1030sh	ν (W=O)
785s	ν (O-W-O)	754vs	ν (O-W-O)
595w	ν_4 (PO_4)	/	
426w	ν (W-PO_4)	415w	ν (W-PO_4)

Marks: vs-very strong, s-strong, m-medium, w-weak, sh-shoulder

Table IV. Comparison of the atomic and weight concentrations for Fe-PWA and Fe-PWB. There were presented region and linescan analyses.

Element Symbol	**Fe-PWA region**		**Fe-PWA linescan**		**Fe-PWB region**		**Fe-PWB linescan**	
	Atomic Conc.	**Weight Conc.**	**Atomic Conc.**	**Weight Conc.**	**Atomic Conc.**	**Weight Conc.**	**Atomic Conc.**	**Weight Conc.**
W	57.88	93.67	66.33	95.25	42.84	88.87	43.92	89.23
O	40.46	5.70	31.53	3.94	54.19	9.78	52.92	9.36
P	0.85	0.23	0.67	0.16	1.85	0.65	1.96	0.67
Fe	0.81	0.40	1.47	0.64	1.12	0.71	1.21	0.74

Figures:

Figure 1.

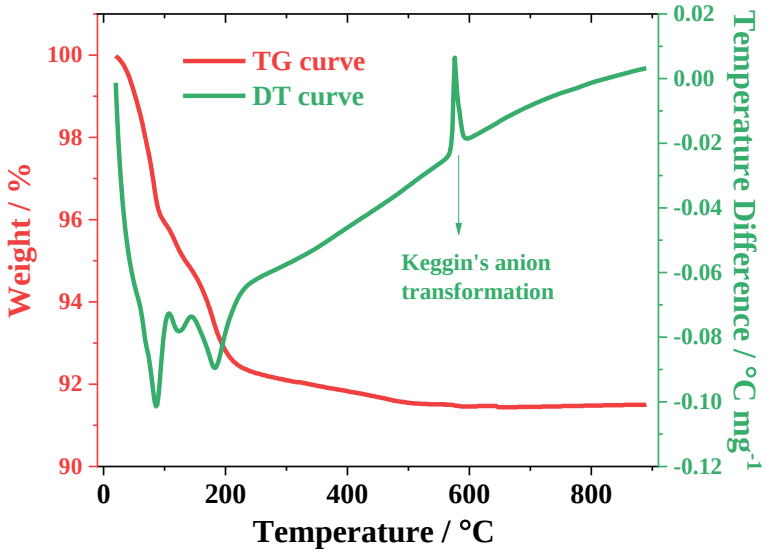

Figure 2.

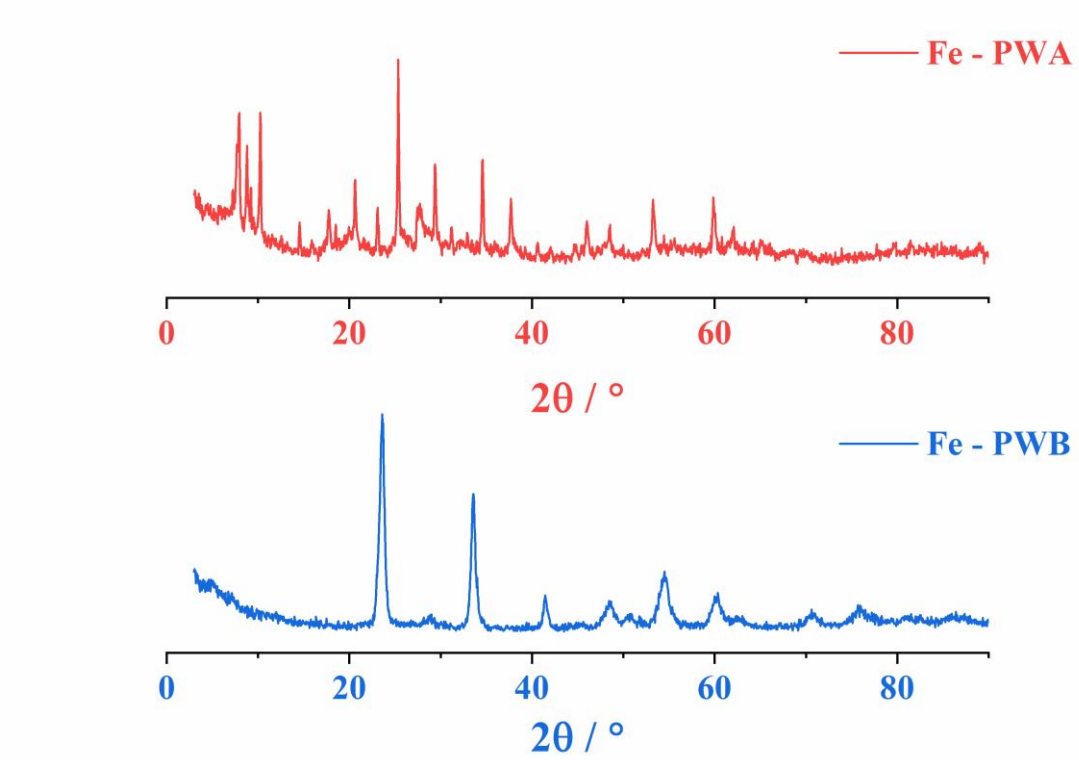

Figure3.

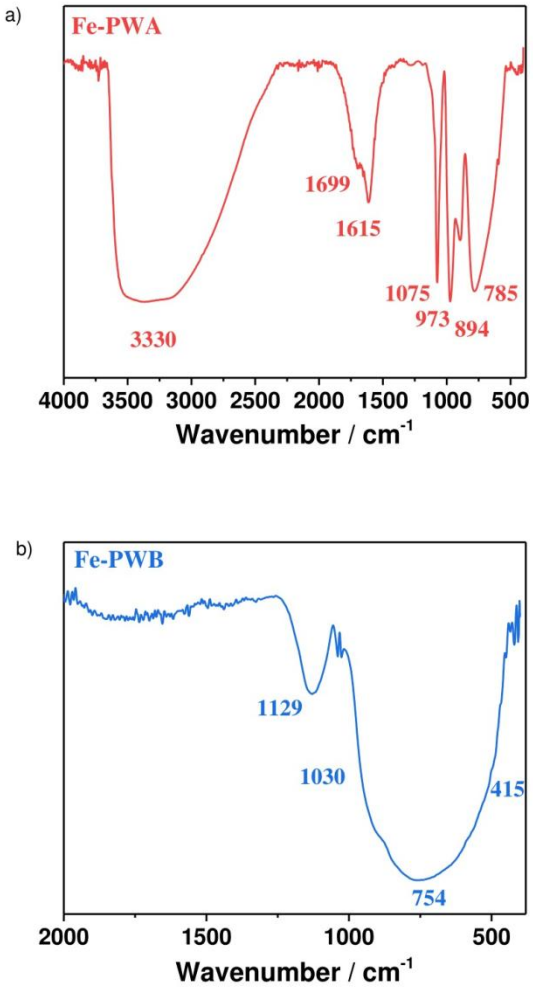
a)
Fe-PWA
1699
1615
1075
973
894
785
3330
4000 3500 3000 2500 2000 1500 1000 500
Wavenumber / cm-1
b)
Fe-PWB
1129
1030
415
754
2000 1500 1000 500
Wavenumber / cm-1

Figure 4.

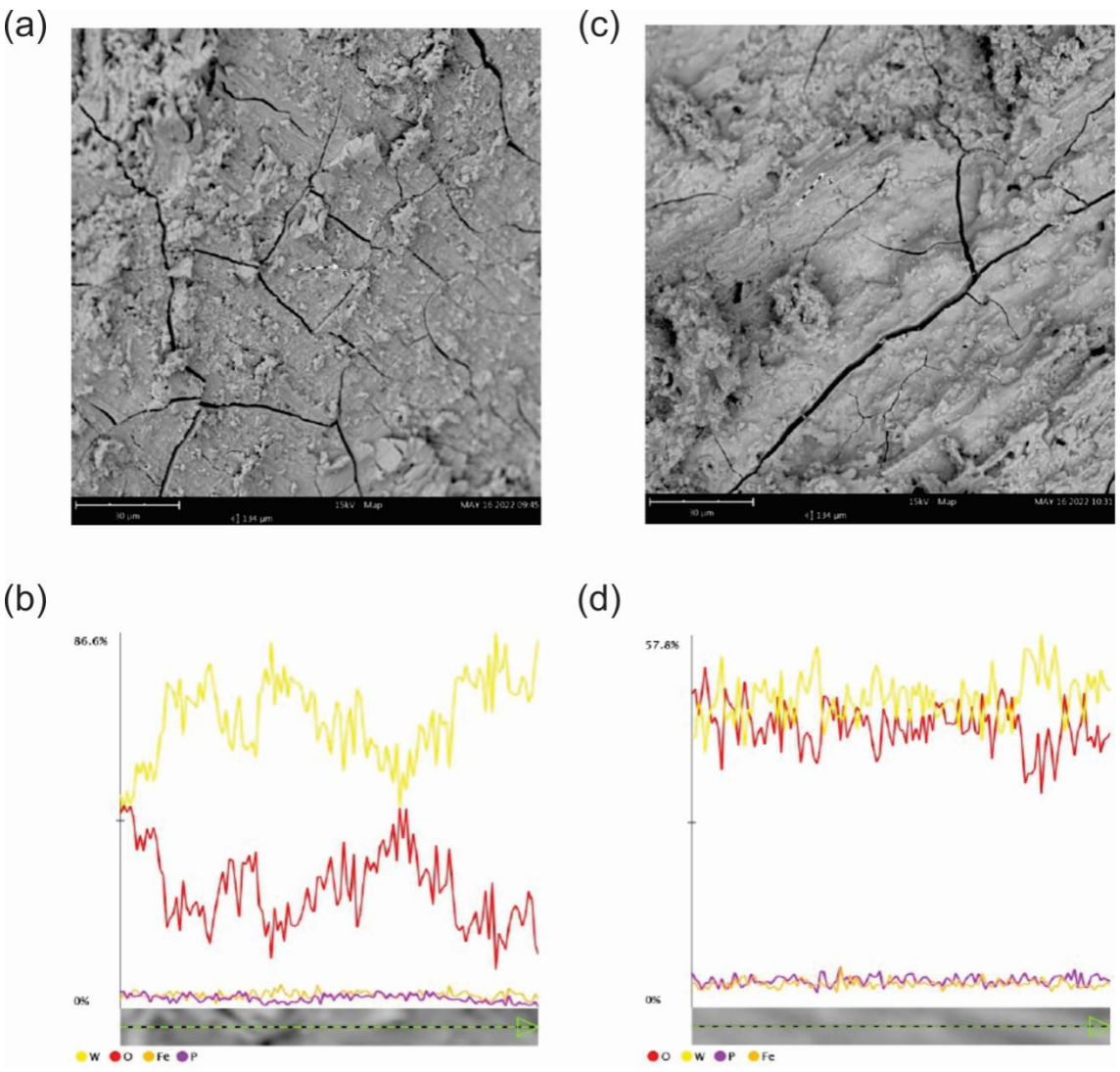

Figure 5.

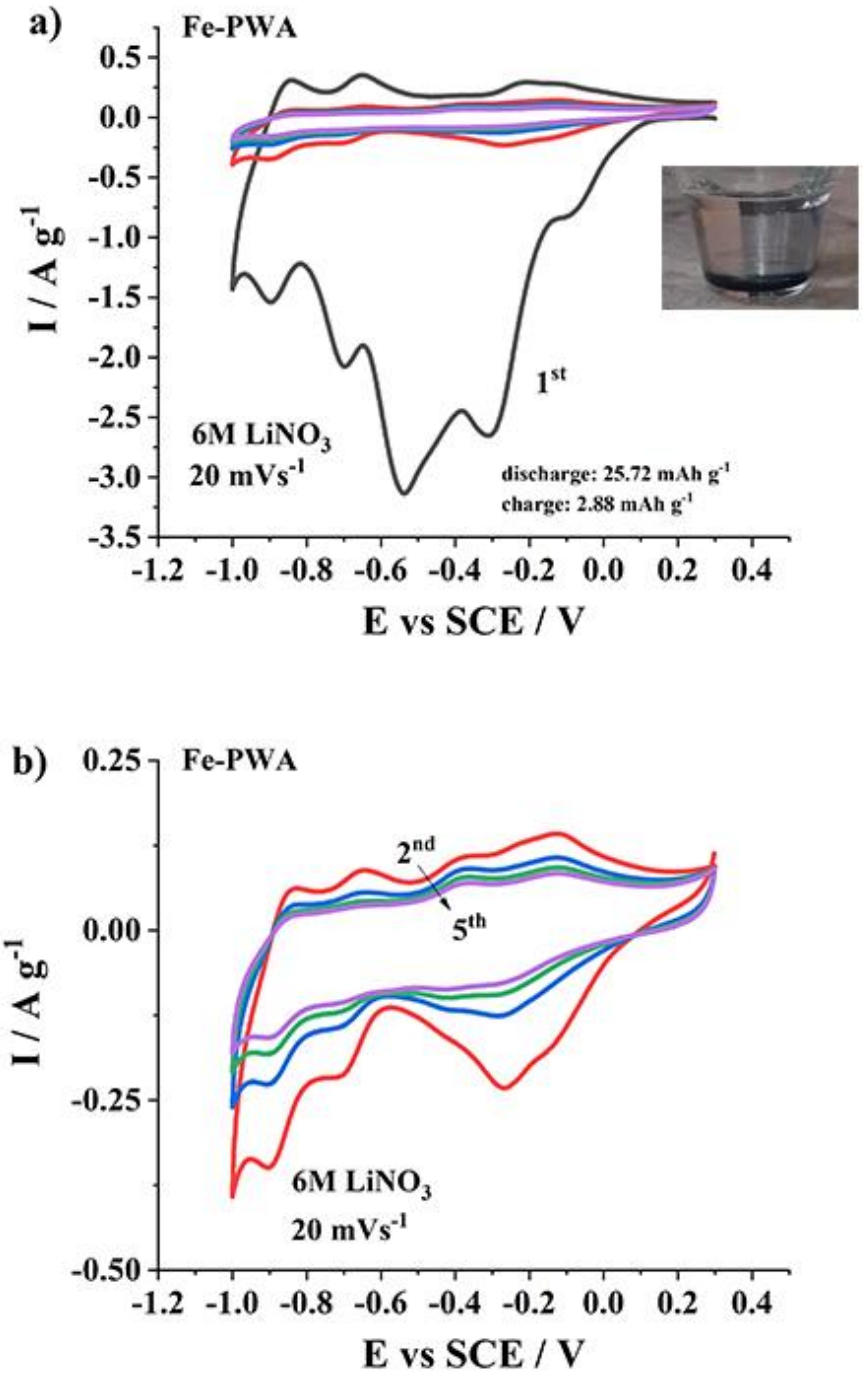
a)
Fe-PWA
I / A g-1
E vs SCE / V
1st
6M LiNO3
20 mVs-1
discharge: 25.72 mAh g-1
charge: 2.88 mAh g-1
b)
Fe-PWA
2nd
5th
6M LiNO3
20 mVs-1

Figure 6.

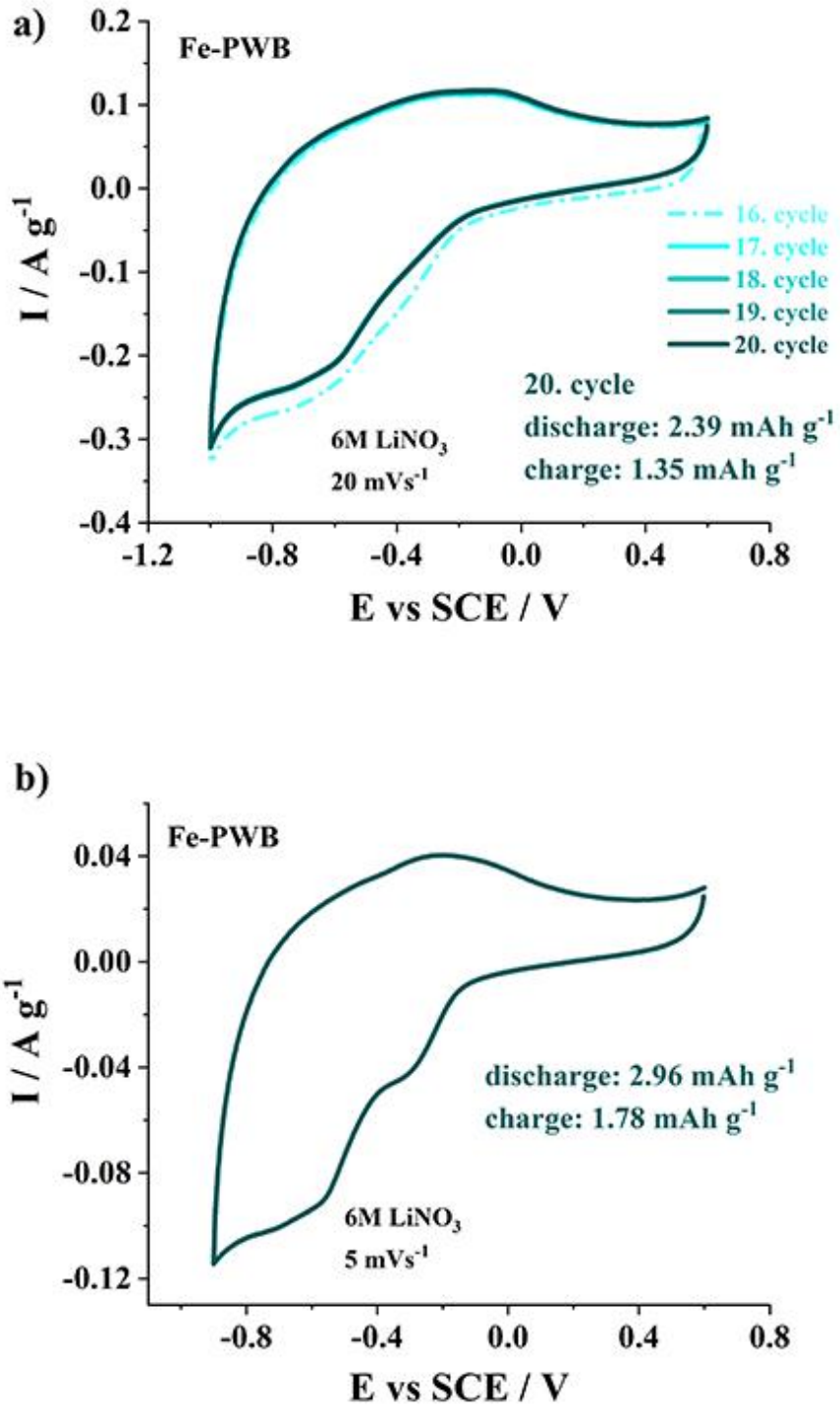
a)
Fe-PWB
0.2
0.1
0.0
-0.1
-0.2
-0.3
-0.4
I / A g-1
16. cycle
17. cycle
18. cycle
19. cycle
20. cycle
20. cycle
discharge: 2.39 mAh g-1
charge: 1.35 mAh g-1
6M LiNO3
20 mVs-1
-1.2
-0.8
-0.4
0.0
0.4
0.8
E vs SCE / V
b)
Fe-PWB
0.04
0.00
-0.04
-0.08
-0.12
I / A g-1
discharge: 2.96 mAh g-1
charge: 1.78 mAh g-1
6M LiNO3
5 mVs-1
-0.8
-0.4
0.0
0.4
0.8
E vs SCE / V

Сажетак: *У овом раду синтетисана је 12-волфрам фосфорна киселина ($H_3PW_{12}O_{40} \times nH_2O$; PWA), која је даље јонски допирана са Fe^{3+} јонима, што је довело до формирања соли гвожђа 12-волфрам фосфорне киселине Fe-PWA соли ($FePW_{12}O_{40} \times nH_2O$). Fe-PWA је затим испитан помоћу термијске анализе (TGA/DTA), фазни прелаз Fe-PWA одиграва се на температури од 576 ^oC, формирајући фосфат волфрамову бронзу допирану гвожђем Fe-PWB. Применом метода дифракције рендгенских зрака на праху, инфрацрвене спектроскопије са Фуријеовом трансформацијом и скенирајуће електронске микроскопије уз енергетску дисперзивну рендгенску спектроскопију, добијени Fe-PWB је додатно карактерисан, чиме је потврђена жељена структура. Због канала и шупљина у њиховим структурама, Fe-PWA и Fe-PWB су затим испитани као електродни материјали за пуњиве батерије. Електрохемијска мерења вршена су у воденим растворима 6M $LiNO_3$ цикличном волтаметријом. Електрохемијски резултати показују да унутар структуре Fe-PWA, више Li^+ јона може бити интеркалирано у првом циклусу пражњења, али даље циклирање доводи до брзог смањења капацитета. Док је редокс процес Fe-PWB био стабилан током циклирања, његов специфични капацитет је ограничен слабом електричном проводљивошћу материјала. Специфични капацитет Fe-PWB је скоро незнатан, па је неопходно оптимизовати његове физичко-хемијске особине како би се вредност његовог специфичног капацитета повећала. Побољшање проводљивости Fe-PWB биће истраживана у будућим студијама, како би се побољшале електрохемијске перформансе материјала.*

***Кључне речи**: хетерополи киселине, гвожђе фосфат волфрамова бронза, Кегинов анјон, циклична волтаметрија, реакција интеркалације/деинетеркалације литијума*